Modeling of Surface Crack Defects Developed on Shear Edge in High-strength Automotive Steel Sheets

Sota GOTO,[1)]* Kazuhiko YAMAZAKI,[2)] Thi-Huyen DOAN,[1)] Yoshimasa FUNAKAWA[3)] and Osamu UMEZAWA[4)]

1) Steel Research Laboratory, JFE Steel Corporation, 1-1 Minamiwatarida-cho, Kawasaki-ku, Kawasaki, 210-0855 Japan.
2) Steel Research Laboratory, JFE Steel Corporation, 1 Kawasaki-cho, Chuo-ku, Chiba, 260-0835 Japan.
3) Sheet Business Planning Dept., JFE Steel Corporation, 2-2-3 Uchisaiwai-cho, Chiyoda-ku, Tokyo, 100-0011 Japan.
4) Faculty of Engineering, Yokohama National University, 79-5 Tokiwadai, Hodogaya-ku, Yokohama, 240-8501 Japan.

Surface crack defects developed on the shear edge cause a problem in shearing of high-strength steels. The surface crack formation mechanism was clarified by microstructural examinations and numerical simulation. Two types of 780 MPa grade hot-rolled steel sheets with a thickness of 2.6 mm were chosen for the evaluations because the materials show different surface crack susceptibilities. Cleavage fracture was responsible for the surface cracks, and micro-ductile cracks with a length of 30 μm to 40 μm were detected in the interrupted punching samples. A numerical simulation demonstrated that a tensile stress was developed in the direction of the micro-ductile cracks opening during punching process. The critical length of the micro-ductile crack for cleavage fracture as a crack initiation site was given by linear fracture mechanics; for example, the critical length is 23 μm or longer under the applied tensile stress of 910 MPa. The tensile stress causing cleavage fracture decreased by reducing the tool clearances, and it was shown experimentally that surface crack defects can be prevented by controlling the clearance appropriately.

KEY WORDS: 780 MPa grade hot-rolled steel; hole punching; cleavage fracture; micro-ductile crack; GTN model.

1. Introduction

High-strength steel sheets have been applied to automotive components to reduce car weight while ensuring collision resistance and fatigue endurance. However, the shear edge properties of high-strength steels deteriorate due to surface cracks that develop in the fractured area of the shear edge. In experimental and simulated tensile testes, Dalloz *et al.*[1] demonstrated that surface cracks of this type lowered the ductility of dual-phase steels because the crack area deformed preferentially. Shih *et al.*[2] called these surface cracks "3-D formations" and related the cracks to degeneration of hole expanding formability caused by the high roughness of the shear edge. Regarding the fatigue property of punched holes of high-strength steels, the roughness of the shear edge, including surface cracks, is a negative influencing factor on fatigue strength in addition to the residual stress of the punched edge.[3,4] The surface cracks are often rejected as appearance defects. This is because the surface cracks vary in size and it is difficult to predict the influence of the surface cracks on the shear edge properties.

Although surface cracks affect the formability, performance, and appearance quality of automotive components in which high-strength steel sheets are used, the surface crack formation process is not well understood. Okano *et al.*[5] attempted to clarify the formation process by observing samples obtained by interrupted punching tests. They supposed that a void initiated at a TiN inclusion propagates into the adjacent matrix grains by cleavage and may lead to the formation of a surface crack, but did not clarify whether the stress state which develops during the punching process can cause the cleavage.

Several approaches by numerical simulations such as the Lamaitre damage model,[6] Gurson damage model,[7] and fully coupled damage model[8] have been used to estimate the shape of the shear edge. These simulations mostly focused on cutting behavior during the punching process. Although the relationship between the propagation path of the ductile crack and the equivalent strain/equivalent stress has been examined extensively, the principal stresses developed, which are responsible for the cleavage fracture, have not yet been clarified.

The present study addresses the problem of understanding the formation process of surface cracks on the shear edge in high-strength steel sheets by experimental and numerical simulation. A round hole punching process is adopted for modelling of shearing, and an experimental analysis of the surface crack phenomenon is carried out to clarify the fact that cleavage fracture causes surface crack. In the numerical simulation, the focus is the principal stress which develops in the direction of the surface crack opening, and the criteria

of the cleavage fracture are discussed. Finally, the influence of the punching clearance on the sheared edge condition is clarified.

2. Experimental Analysis of Surface Crack

2.1. Experimental Procedure

In order to define the fracture morphology of surface cracks, punching tests and microstructural observations were carried out. Interrupted punching tests were also conducted to examine when the surface cracks developed during the punching process.

The punching tests were conducted with the hole punching die set (Miyagi, A-1-150 type) schematically illustrated in **Fig. 1**(a). The punch diameter D_p and the die diameter D_d were 10 mm and 11 mm, respectively, and the clearance of the punch and die c was 0.5 mm. Punching was performed with a press machine (Komatsu Industries, OBS25-2) having a press speed of 125 shots per minute. The stroke of the press machine was 80 mm, and the speed of the punch on reaching the sample surface was calculated to be 200 mm/s. No lubricant was used. The sample size for the punching tests was 30 mm square and a thickness of 2.6 mm, as shown in Fig. 1(b).

The surface cracks that developed on the shear edge were observed with a scanning electron microscope (SEM, Hitachi High-Technologies SU5000). The surface crack propagation plane was characterized by the electron backscatter diffraction (EBSD) method with a charge coupled device camera (EDAX, Hikari EBSD Camera). For the EBSD, the samples were finally polished with a diamond paste having a diameter of 0.25 μm and finished for 15 min with a colloidal silica suspension. The step size of the EBSD measurement was 0.1 μm. The EBSD was analyzed by OIM Analysis^{TM} software.

For the punching tests, two types of 780 MPa-grade C-Mn hot-rolled steel sheets with a thickness of 2.6 mm were used. One was a precipitation-hardened ferritic steel (steel A) having yield strength of 767 MPa, tensile strength of 824 MPa, uniform elongation of 10%, and total elongation of 21%. The other was a transformation-hardened steel (steel B) having yield strength of 727 MPa, tensile strength of 807 MPa, uniform elongation of 7%, and total elongation of 17%. The mean grain diameters of steel A and steel B were

3.4 μm and 2.4 μm, respectively. The mean grain diameters were evaluated by converting the number-averaged grain diameter automatically calculated by OIM Analysis to the equivalent circle diameter, and the grain boundary was defined by a misorientation angle of 15° or more.

The interrupted punching test was also carried out with the same die set as that used for the punching test. The stroke displacement for interrupting punch penetration was determined by the following steps: (1) The stroke displacement at which the punch made contact with the sample surface was defined as the reference position, (2) the stroke displacement was then increased by 0.1 mm from the reference position until cutting of the material was completed and (3) the interruption displacement was determined to be a displacement 0.1 mm smaller than the displacement at which the cutting was completed. The interruption displacements were 1.8 mm for steel A and 1.7 mm for steel B.

2.2. Fracture Morphology of Surface Crack

Figure 2 shows micrographs of the shear edges of steel A and steel B. Surface cracks were observed in both steel A and steel B, but the surface cracks in steel A were larger than those in steel B. **Figure 3** shows a cross-sectional image of the surface cracks in steel A. The surface cracks
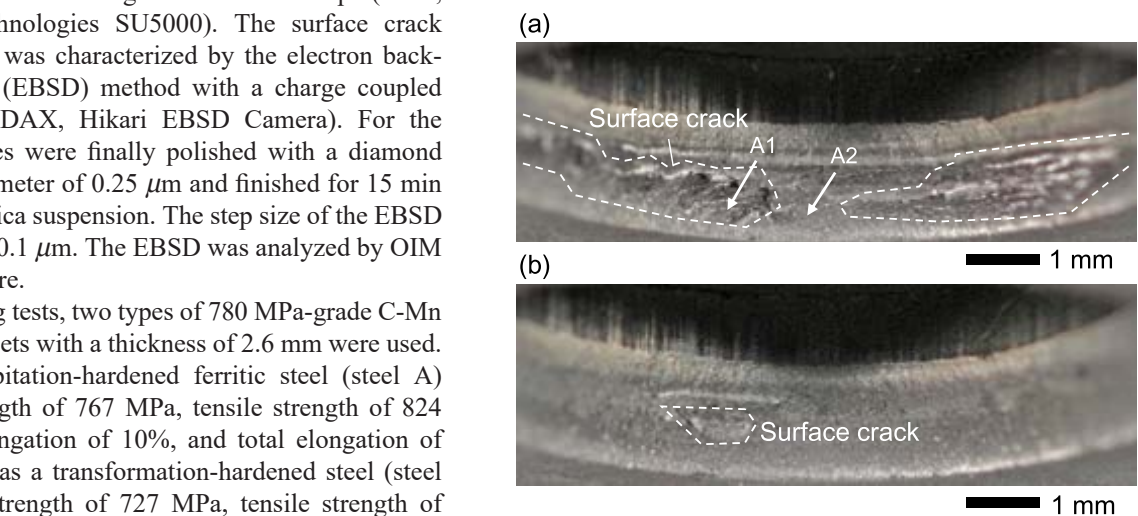

Fig. 2. Micrographs of shear edge of (a) steel A and (b) steel B punched with clearance of 0.5 mm. (Online version in color.)
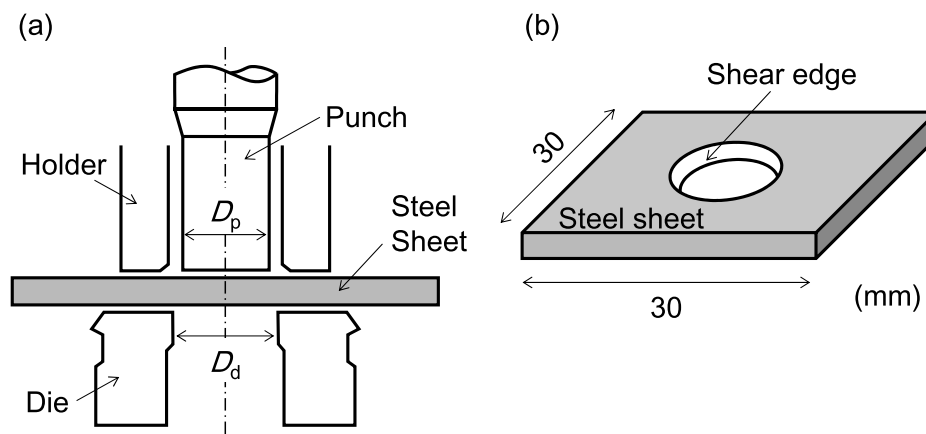

Fig. 1. Schematic illustration of (a) punch and die set and (b) punched sample.

propagated from the shear edge into the material, which was similar to the morphology called "3-D formations" by Shih.[2] The maximum length of the surface cracks observed was approximately 200 μm.

Figures 4(a) and 4(b) show fractographs of the surface crack at A1 in Fig. 2(a), and Fig. 4(c) shows a fractograph of the normal fractured area at A2 in Fig. 2(a). The surface cracks showed the brittle fracture with river pattern, while the normal fractured area showed a ductile fracture with dimples. Dimples with inclusions elongated along the punching direction, as indicated by black arrows in Fig. 4, were observed on the brittle fracture surface. The dimples with inclusions were also observed on the normal fracture

surface, but their sizes were smaller than those observed on the brittle fracture surface. **Figure 5** is an EBSD analysis result showing the relationship between the surface crack propagation and crystal orientations. Each red line in Fig. 5 represents a perpendicular to the {001} cleavage plane.
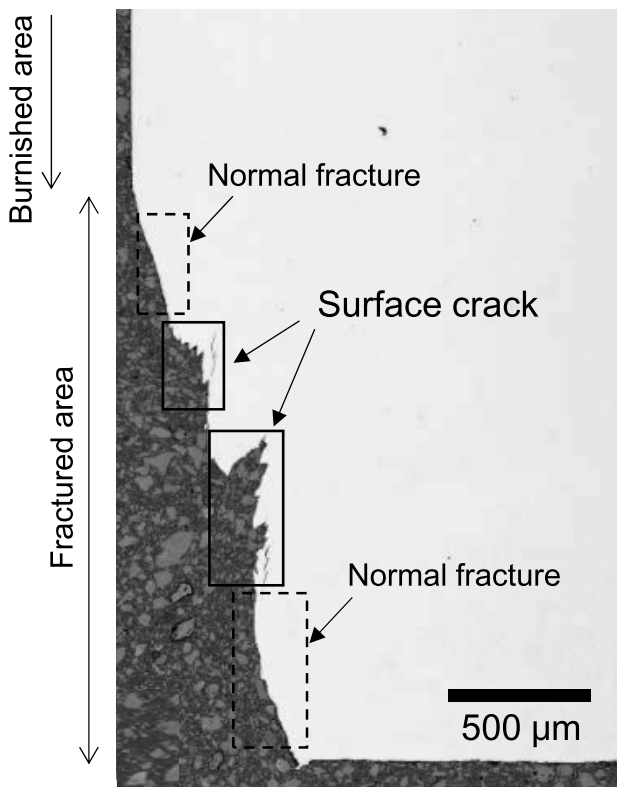

Fig. 3. Morphology of surface crack observed in steel A.
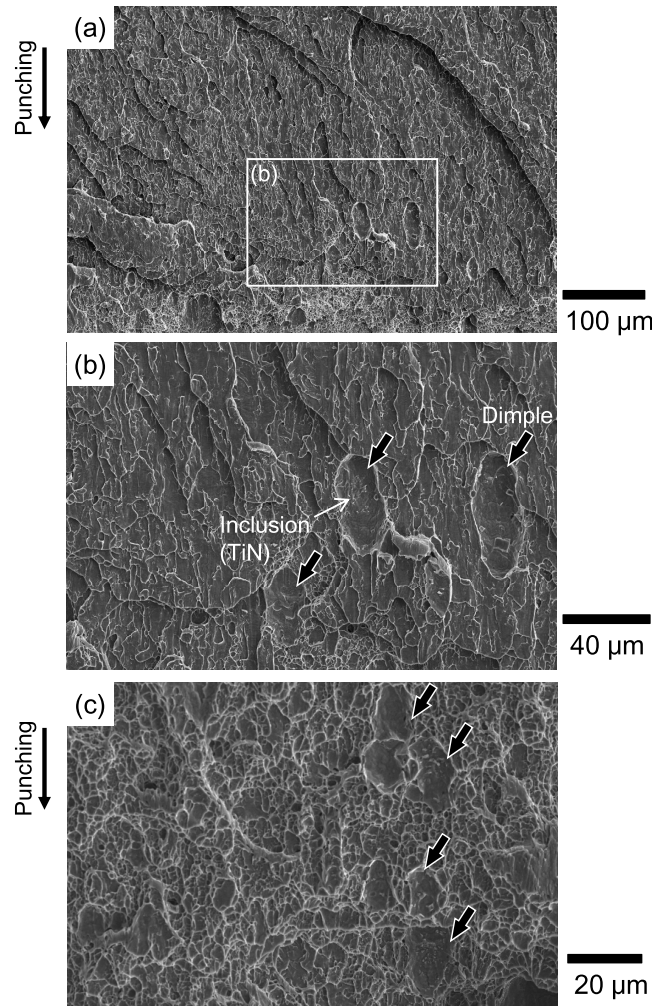

Fig. 4. Fractographs of (a) surface crack area with low magnification, (b) surface crack area with high magnification, and (c) normal fracture area in steel A.
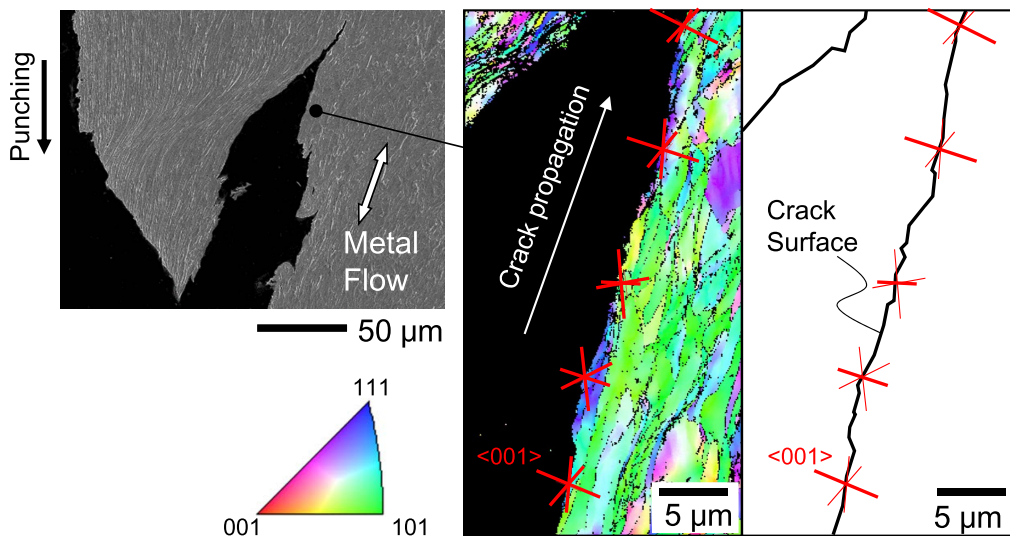

Fig. 5. Relationship between crack surface and (001) cleavage plane in steel A. (Online version in color.)
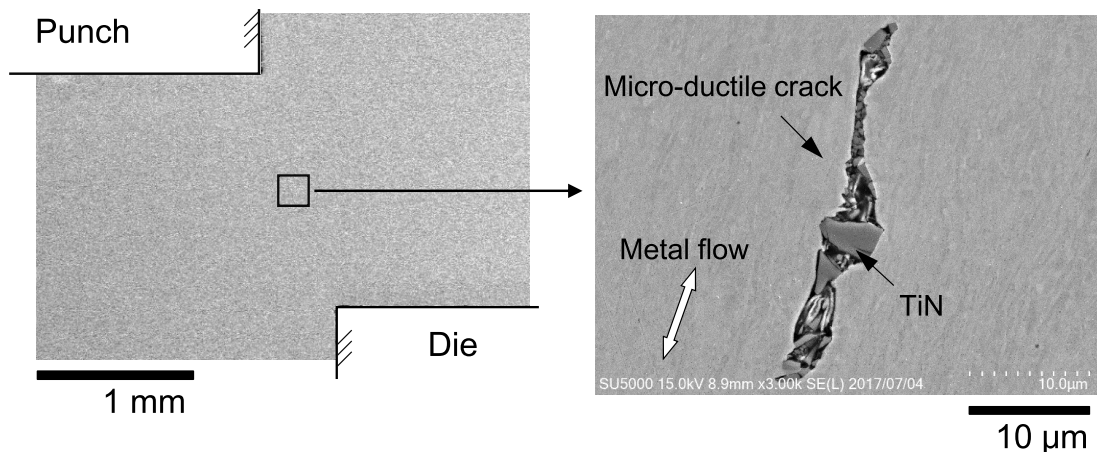
Fig. 6. Cross-sectional scanning electron micrographs of interrupted punching sample in steel A (Interruption displacement: 1.8 mm).

The normal lines of the {001} cleavage plane were almost orthogonal to the plane of the crack. From the above observation and analysis, the present authors concluded that the surface cracks on the shear edge developed by cleavage.

Figure 6 shows a cross-sectional micrograph of the interrupted punching sample of steel A. A micro-ductile crack containing fragmented TiN inclusions was observed, but no large cracks with a length of 200 μm were observed. The length of 200 μm was the maximum length of the surface cracks observed in Fig. 3. Figure 6 indicates that surface cracks develop within a very short period of the cutting of the material.

A ductile fracture in steel begins with void nucleation at a site in which plastic strain concentrates. In a study of Ti-bearing IF steel, León-Garcia et al.[9] reported that a TiN inclusion became a void nucleation site during tensile deformation. They observed that the void nucleated by either separation of the inclusion-matrix interface or by fragmentation of the inclusion. Since the micro-ductile crack in the present study also contained fragmented TiN inclusions and initiated along the metal flow, the micro-ductile crack observed in the interrupted punching sample was produced as a result of the plastic deformation that occurred during punching, and was different from a surface crack caused by cleavage.

In spheroidized steels, ductile voids initiated from carbides at low plastic strain.[10,11] In addition, MnS inclusions,[12] pearlite islands in ferrite-pearlite steel,[13] and martensite islands in dual-phase steel[1] have been reported as ductile void nucleation sites. Thus, not only a TiN inclusion but also such carbides, inclusions, and secondary phases will be the initiation sites of micro-ductile cracks under the plastic deformation in punching.

Figure 7 shows the length distribution of the micro-ductile cracks measured in 10 interrupted punching samples each for steel A and steel B. The interrupted displacements immediately before cutting is completed are 1.8 mm for steel A and 1.7 mm for steel B. Approximately 50 micro-ductile cracks in total were found for each steel. Most of the lengths of the micro-ductile cracks were less than 20 μm, but the maximum lengths were 40 μm in steel A and 32 μm in steel B.
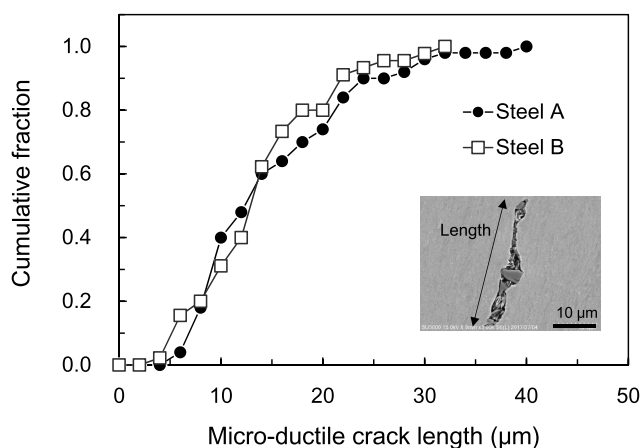

Fig. 7. Micro-ductile crack lengths observed in interrupted punching samples (Measured in 10 samples each).

3. Numerical Simulation of Punching Process

Surface cracks developed by cleavage fracture, as shown in Figs. 4 and 5, and cleavage fracture is primarily controlled by the stress state.[14] Therefore, a numerical simulation by finite element analysis (FEA) was performed in order to check whether stress develops in the direction of surface crack opening.

3.1. Determination of Material Parameters

The stress-strain relations for the two steels were approximated by Eq. (1). It may be noted that Eq. (1) was used for the strain range after uniform elongation instead of the experimental stress-strain curves:

$$\sigma = Y + K\varepsilon^{N} \quad \cdots\cdots\cdots\cdots\cdots (1)$$

where, Y, K, and N are material constants. Each value of Y, K, and N for steel A and steel B is listed in **Table 1**. Since punching was carried out under a high strain rate of 10^3/s, the effect of the strain rate on the stress-strain relation should be taken into account. Low-temperature tensile tests at a temperature in the range of $-80°C$ to $-196°C$ were performed to determine the change in yield strength at several strain rates. Subsequently, the test temperatures were converted to the strain rate by using the rate-temperature

parameters (Eq. (2)[15]). Then, an increase of yield strength at 10^3/s was incorporated in Eq. (1).

$$R = T \ln\left(\frac{C}{\dot{\varepsilon}}\right) \quad \text{............................... (2)}$$

where, T is the test temperature in Kelvin degree and C is a material constant (10^8 s^{-1}).

Figures 8(a) and 8(b) show the variation of yield strength (σ_{ys}) as a function of the test temperatures and the increase of yield strength against the strain rates, respectively. σ_{ys0} represents the yield strength measured at ambient temperature with a strain rate of 10^{-3} s^{-1}.

The cleavage fracture criteria of the investigated steels were determined by low-temperature three-point bending tests. An out-of-plane bending specimen with a machined v-notch was used. The setup of the bending test is shown in **Fig. 9**. Although the crack opening direction in the three-point bending test and the crack opening direction of the

surface crack were different, the cleavage fracture criteria were determined assuming that the microstructural parameters had no anisotropy, due to experimental constraints.

The bending tests were conducted at −196°C with a punch speed of 5 mm/s. As the result, cleavage fracture occurred in the investigated steels at loads of 2.8 kN for steel A and 4.7 kN for steel B. The fracture loads were evaluated from the average of two measurements. The macroscopic cleavage fracture stresses were determined by calculating the principal stress underneath the v-notch at the fracture loads by FEA (code: Abaqus/Standard). Consequently, the cleavage fracture stresses for steel A and steel B were 2 351 MPa and 2 546 MPa, respectively. The stress triaxialities defined as the ratio of mean stress to equivalent stress were 1.94 for steel A and 1.45 for steel B when cleavage occurred.

As an elementary step of cleavage fracture in steels consisting of ferrite-cementite, the following three stages are proposed:[16,17] Stage 1. Nucleation of a crack at intergranular cementite, Stage 2. Propagation across cementite/ferrite interface of the crack having a length corresponding to the thickness of cementite, and Stage 3. Crack propagation across ferrite/ferrite grain boundary. According to the previous study,[17] crack extension across the cementite/ferrite interface (Stage 2) is the critical stage in cleavage fracture. In the present study, however, the authors assumed that cleavage fracture of the investigated steels was controlled by

Table 1. Material constants of investigated steels for approximated stress-strain relation.

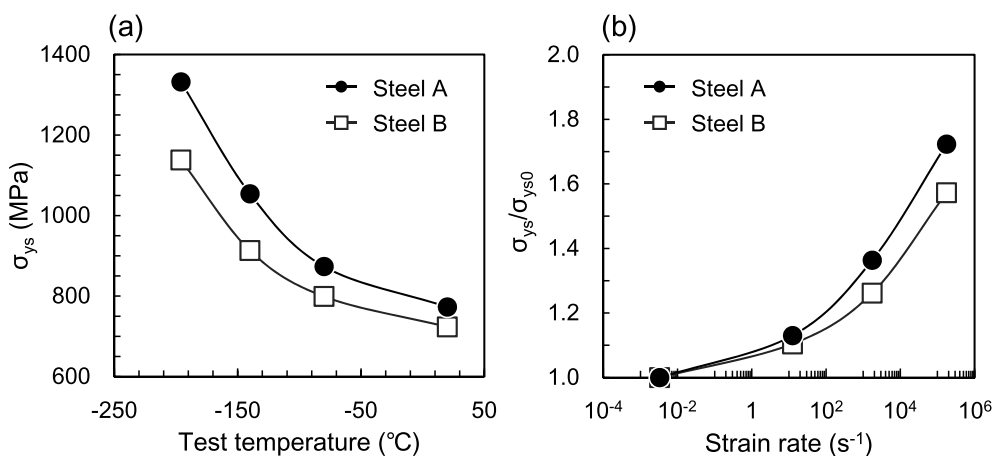| Material	$\sigma = Y + K\varepsilon^N$ (at 10^{-3} s^{-1})			Strain range	Stress ratio at 10^3 s^{-1}
	Y	K	N		σ_{ys}/σ_{ys0}
Steel A	750	646	0.591	$\varepsilon > 0.0953$	1.32
Steel B	641	513	0.300	$\varepsilon > 0.0677$	1.23

Fig. 8. (a) Relationship between yield strength and tensile test temperature and (b) relationship between stress ratio, σ_{ys}/σ_{ys0} and strain rate converted from test temperature by using Eq. (2).
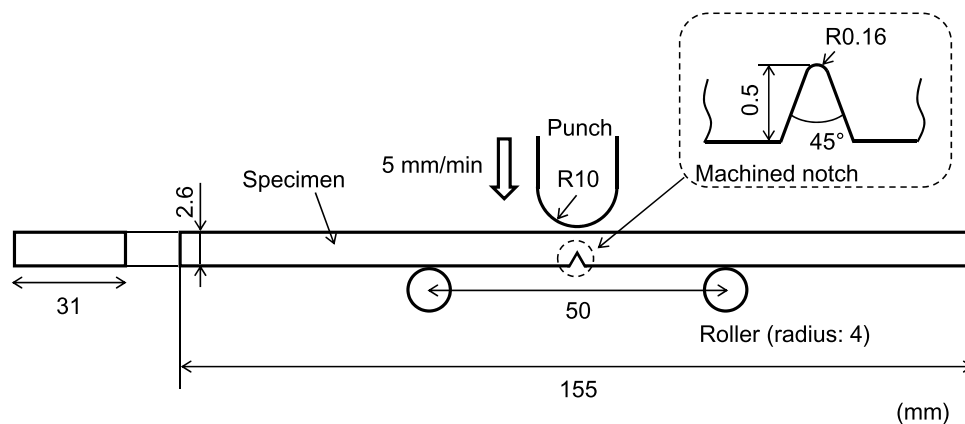

Fig. 9. Specimen geometry and its setting for v-notched bending test.

Stage 3 because steel A contains no intergranular cementite and steel B contains only extremely-thin intergranular cementite with a thickness of less than 0.1 μm. For Stage 3, the macroscopic cleavage stress σ_f is given using the Griffith equation in terms of the grain diameter D by following equation:[17,18]

$$\sigma_f = \sqrt{\frac{\pi E \gamma_p}{(1-v^2)D}} \quad .... (3)$$

where E is the Young's modulus (206 GPa), v is the Poisson's ratio (0.3), and γ_p is the effective surface energy. The effective surface energy can be estimated using the macroscopic cleavage stresses determined by the previous three-point bending test (2 351 MPa for steel A, and 2 546 MPa for steel B) and the mean grain diameters measured by the EBSD method. Substituting these values into Eq. (3), the effective surface energies for steel A and steel B were calculated as 27 J/m^2 and 22 J/m^2, respectively. San Martin et al.[19] experimentally determined the effective surface energy of Ti–V microalloyed steel at -196°C in Stage 3, and reported that the value was 50 J/m^2. They also showed that the effective surface energies were almost constant at temperatures of -196°C to -70°C. From Eq. (2), deformation with the strain rate 10^3/s at ambient temperature in the punching process is equivalent to the static deformation at a temperature of -134°C. For this reason, in the present study, the effective surface energies determined by the three-point bending test at a test temperature of -196°C were used as cleavage fracture parameters in the punching process.

3.2. Damage Evolution Equation for Finite Element Analysis

Material separation in the punching process is normally caused by ductile fracture involving void growth and coalescence. The void growth rate for an increment of plastic strain is strongly influenced by hydrostatic stress.[20] Gurson[21] expressed the deformation behavior of a metal including a void by means of a damage evolution equation considering the effects of the equivalent stress, the hydrostatic stress, and the volume fraction of the void. The Gurson model modified by Tvergaard[22,23] and Tvergaard and Needleman[24] was applied to the present FEA of the punching process. The damage evolution equation is given by Eq. (4):

$$\Phi = \left(\frac{\sigma_{eq}}{\sigma_{ys}}\right)^2 + 2q_1 f \cosh\left(\frac{3q_2\sigma_m}{2\sigma_{ys}}\right) - (1+q_3 f^2) = 0 \quad ... (4)$$

where, σ_{eq}, σ_m, σ_{ys}, and f are the von Mises equivalent stress, the mean stress, the yield strength of the material, and the volume fraction of the void, respectively. The constants q_1, q_2, and q_3 are added to the Gurson equation by Tvergaard,[22]

and their values are 1.5, 1.0, and 2.25, respectively. The void nucleation rate was expressed by the strain-controlled model given by Eq. (5):

$$\dot{f}_{nucleation} = \frac{f_N}{S_N \sqrt{2\pi}} \exp\left\{-\frac{1}{2}\left(\frac{\varepsilon_m^p - \varepsilon_N}{S_N}\right)^2\right\}\dot{\varepsilon}_m^p \quad .... (5)$$

where, $\dot{\varepsilon}_m^p$ is the increment of equivalent plastic strain, ε_N is the strain at which a void nucleates, S_N is the standard deviation of ε_N ($= 0.1$), and f_N is the volume fraction of the voids at ε_N. The parameters ε_N and f_N were determined by comparing the experimental result and FEA (code: Abaqus/Standard) results of the uniaxial tensile test. On the other hand, the parameters for void growth, f_c and f_f, were determined by comparing the experimental and FEA (code: Abaqus/Explicit) results of punching. All damage parameters for steel A and steel B in the present study are summarized in **Table 2**.

3.3. Numerical Simulation Model

Figure 10 shows the initial finite element mesh for the FEA of the punching process. The model is a two-dimensional axisymmetric model. The thickness of the steel sheet $t = 2.6$ mm, the diameter of the punch $D_p = 10$ mm, and the clearance between the punch and die $c = 0.5$ are the same as the experiment conditions. The diameter of the steel sheet was 100 mm, and the radii of the edges of the punch and die were 0.01 mm. The mesh was divided into 120 elements of CAX4RT in the thickness direction, and the total element count of the steel sheet was 13 680.

The punch, die, and holder were regarded as complete rigid bodies. The Young's modulus and Poisson's ratio were 206 GPa and 0.3, respectively. The coefficient of friction between the sample and the tools was 0.2, and the pressure of the holder was 196 kN. The analysis code Abaqus/Explicit was used in order to deal with the punching process with large deformation and fracture over a short period of time. An adaptive mesh[25] was applied to prevent extreme deformation of the elements.

3.4. Numerical Simulation Results

Figure 11 shows the cross-sectional shape of the simulated shear edge of steel A. The lengths of the burnished area and fractured area showed good agreement with the experimental results. Since the tools were regarded as
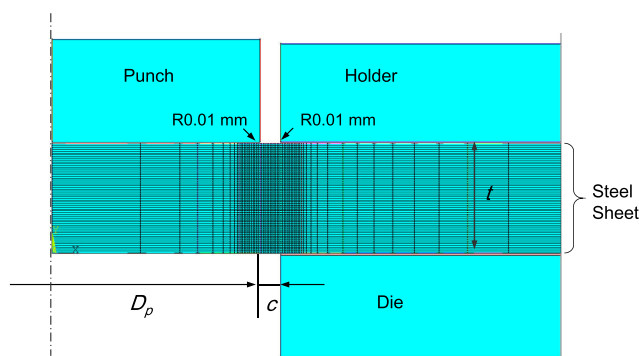
Table 2. Damage parameters of steel A and steel B.

Material	ε_N	f_N	f_c	f_f
Steel A	0.3	0.015	0.08	0.10
Steel B	0.6	0.005	0.10	0.12

Fig. 10. Initial finite element mesh for FEA of punching process (Mesh type: CAX4RT, total element count: 13 680). (Online version in color.)

complete rigid bodies, material separation was already completed at the punch penetration of 1.5 mm in the FEA simulation. **Figures 12**(a)–12(d) show contour plots for the
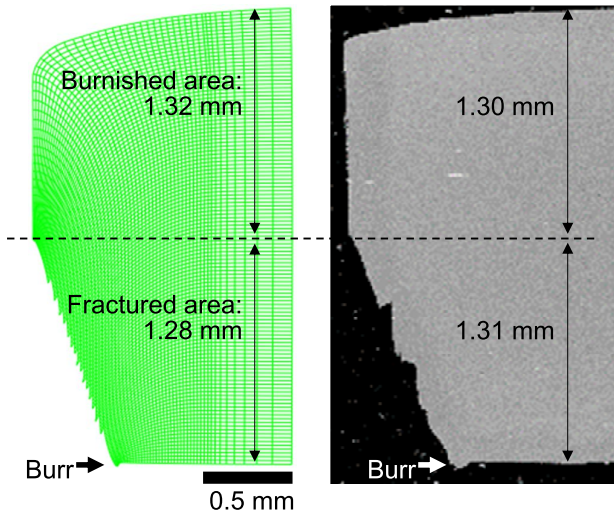
equivalent plastic strain, the stress triaxiality, the maximum principal stress, and the minimum principal stress at the punch penetration of 1.4 mm, respectively. The maximum of stress triaxialities was 1.07 for steel A and 0.83 for steel B. **Figure 13** shows a vector map of the maximum principal stress σ_1 and the minimum principal stress σ_3 at the punch penetration of 1.1 mm. σ_1 developed in the direction that coincides with the metal flow, and σ_3 developed perpendicularly to the metal flow. Therefore, if σ_3 is a tensile component, σ_3 can be the surface crack opening stress because the surface crack undergoes cleavage fracture along the metal flow, as shown in Fig. 5.

Figures 14(a) and 14(b) show the variation of σ_3 at the tracking point shown in Fig. 12(d) during the punching process for steel A and steel B. The tracking point was placed at the mid-thickness of the fractured area, where the surface cracks most likely occurred. The punch penetration at which the load begins to decrease corresponds to the starting point of material separation, and the punch penetration at which the load becomes zero corresponds to the completion point of material separation. At the beginning of punching, the minimum principal stresses σ_3 were negative values, *i.e.* compressive components. Subsequently, σ_3 increased as punching progressed, and turned to positive values, *i.e.*

Fig. 11. Cross-sectional shape of simulated shear edge compared with experimental shear edge in steel A. (Online version in color.)
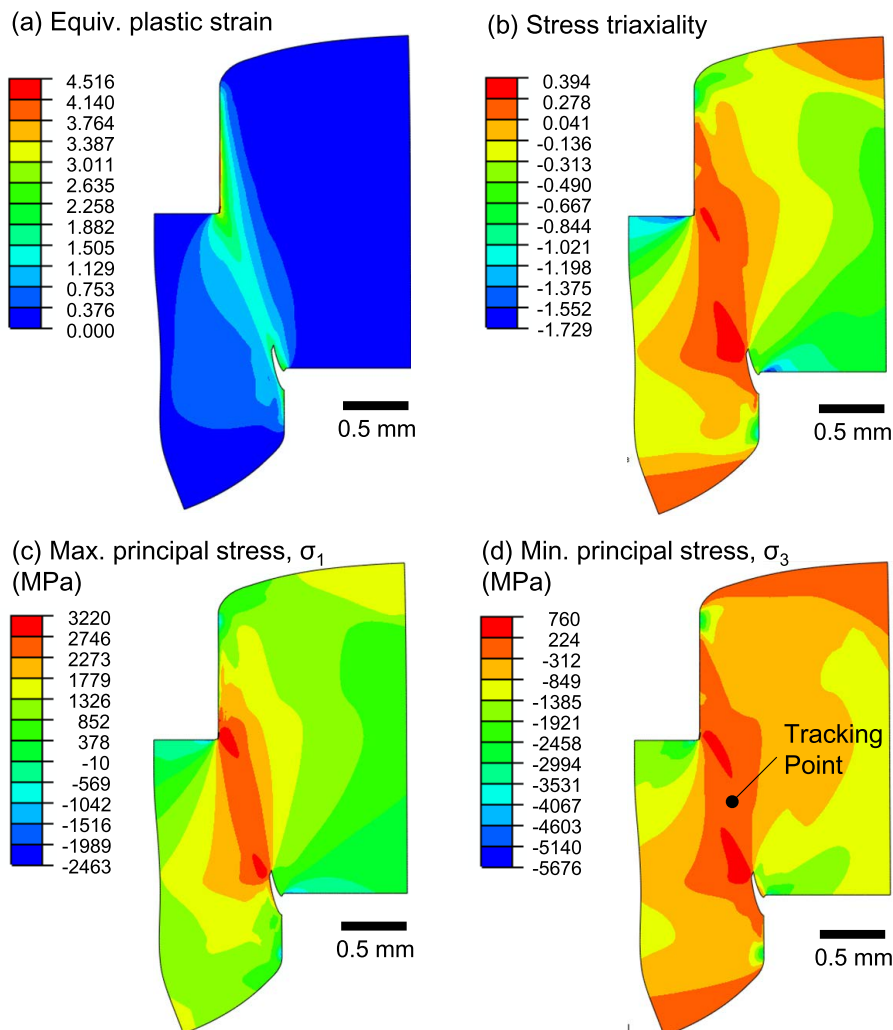

Fig. 12. Contour plots for (a) equivalent plastic strain, (b) stress triaxiality, (c) maximum principal stress, and (d) minimum principal stress at punch displacement of 1.4 mm in steel A. (Online version in color.)
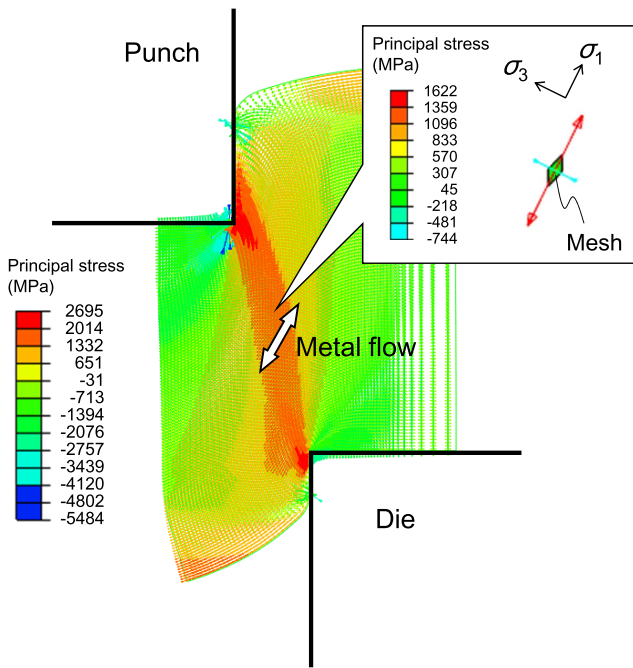
Fig. 13. Vector map of maximum and minimum principal stresses (σ_1 and σ_3) at punch displacement of 1.1 mm in steel A. (Online version in color.)
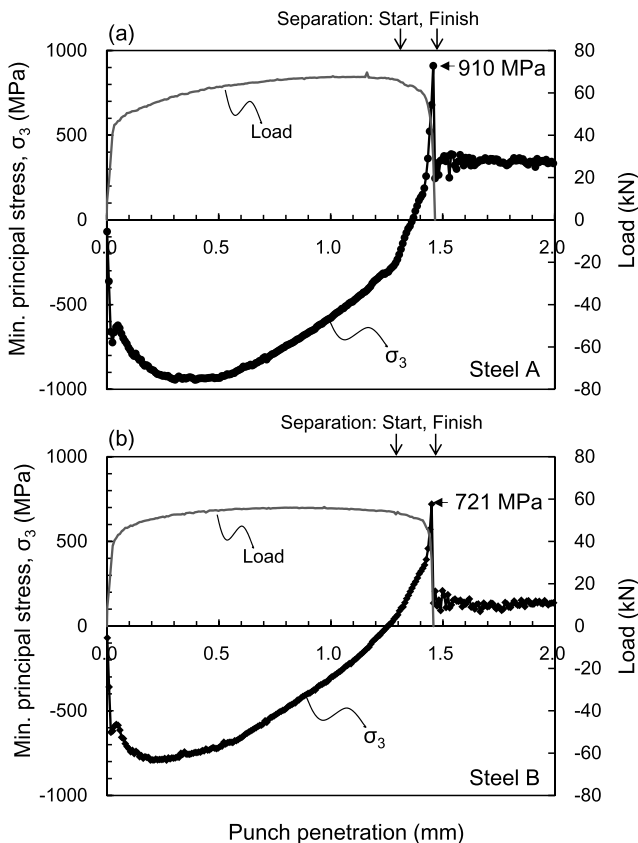

Fig. 14. Variation of minimum principal stress during punching process in (a) steel A and (b) steel B.

tensile components, when material separation started. The numerical simulation confirmed that stress developed in the direction that opened the surface crack after material separation started. σ_3 reached the maximum values of +910 MPa for steel A, and +721 MPa for steel B.

4. Formation Mechanism of Surface Crack Defects

The authors evaluated whether the values of the minimum principal stresses σ_3 obtained by the above numerical simulation are sufficient to cause cleavage fracture. The cleavage fracture stresses of carbon steels are in a range of 2 000 to 2 500 MPa.[19,26,27] In the present study, the cleavage fracture stresses of steel A and steel B were determined to be 2 351 MPa and 2 546 MPa, respectively. In contrast, the values of the σ_3 were calculated to be 910 MPa for steel A and 721 MPa for steel B, which are lower than the cleavage fracture stress in the carbon steel.

Okano *et al.*[5] suggested that origin of surface cracks was Ti compounds. Similarly, in this study, a micro-ductile crack propagates along the TiN compounds as shown in Fig. 6. Then, σ_3 is applied perpendicularly to the longitudinal direction of the micro-ductile crack. The cleavage criterion was examined thereby by treating the micro-ductile crack initiated at TiN as a "pre-existing crack" which causes cleavage fracture.

The minimum length of a micro-ductile crack $2a$ necessary for cleavage fracture was estimated by using the Griffith equation given in Eq. (6) when the stresses σ_3 of 910 MPa and 721 MPa were applied. In the estimation, it was assumed that the micro-ductile cracks were disc-shaped with a radius of a, and the minimum principal stress was sufficiently homogeneous for the micro-ductile crack length. As determined by the three-point bending tests, the effective surface energies γ_p for steel A and steel B are 27 J/m^2 and 22 J/m^2, respectively.

$$\sigma_3 = \sqrt{\frac{\pi E \gamma_p}{2(1-v^2)a}} \quad \text{............................ (6)}$$

From Eq. (6), the minimum length $2a$ of the micro-ductile crack was determined to be 23 μm for steel A and 30 μm for steel B. Consequently, cleavage fracture will occur when σ_3 of 910 MPa and 721 MPa are applied to micro-ductile cracks having lengths of 23 μm and 30 μm, respectively. Such micro-ductile cracks are present in the interrupted punching samples, as shown in Fig. 7. Comparing the critical lengths of the micro-ductile cracks with the result shown in Fig. 7, approximately 10% of the micro-ductile cracks have larger lengths than the minimum length of 23 μm in steel A, while 2% have larger lengths than the minimum length of 30 μm in steel B; that is, steel A contains a larger number of origins of cleavage fracture than steel B contains. This relationship qualitatively accords with the fact that the number of the surface crack defects in steel A were more than that in steel B.

From the results of the experimental observation and numerical simulation, the authors proposed the following mechanism of surface crack defect development, as illustrated in **Fig. 15**. In the initial stage of punching, a micro-ductile crack is generated along the metal flow, where the maximum principal stress σ_1 is tensile and the minimum principal stress σ_3 is compressive (Fig. 15(a)). Once material separation starts, the stress field at the mid-thickness of the fractured area changes to multiaxial, and then tensile component of σ_3 is applied in the direction that causes opening of the pre-existing micro-ductile crack (Fig.

15(b)). Cleavage fracture occurs when the stress field at the tip of the micro-ductile crack satisfies the cleavage criterion expressed by the Griffith equation (Fig. 15(c)). Finally, the cleavage crack appears on the shear edge after punching as a surface crack defect (Fig. 15(d)).
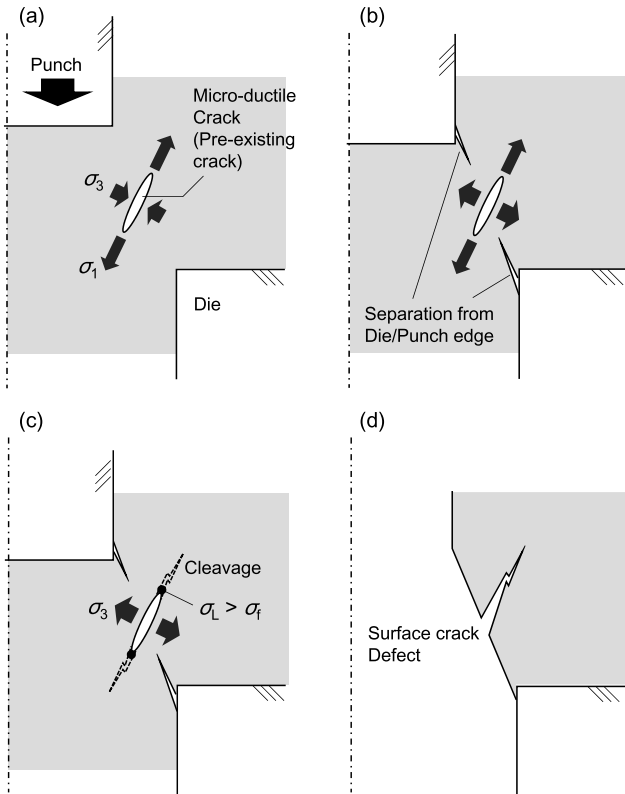
Steel B, which shows fewer surface crack defects than steel A, has the following metallurgical features, as listed in Tables 1 and 2: Smaller increase of yield strength under high strain rate deformation, low strain hardening exponent (N value), and high ε_N and low f_N (high difficulty of micro-void nucleation). These features lead to a reduction in the minimum principal stress σ_3 developed during the punching process, and as a result, the number of surface crack defects in steel B is smaller.

5. Influence of Punching Clearance on Formation of Surface Crack Defect

Figure 16 shows the variations of the minimum principal stress σ_3 in steel B with the clearances of 0.25 mm, 0.5 mm, and 0.8 mm obtained by the FEA simulations. The FEA simulations were performed in the same manner as described in section 3 except for the clearance condition. σ_3 showed the highest value with the clearance of 0.5 mm, and decreased with the clearances of 0.25 mm and 0.8 mm.

Fig. 15. Formation mechanism of surface crack defects: (a) generation of micro-ductile crack along metal flow under uniaxial tensile mode, (b) change of minimum principal stress σ_3 from compressive into tensile mode accompanying start of material separation, (c) occurrence of cleavage fracture when stress field at micro-ductile crack satisfies cleavage criterion (σ_L: stress at micro-ductile crack tip, σ_f: fracture stress), (d) appearance of cleavage fractured crack as surface crack defect after punching.
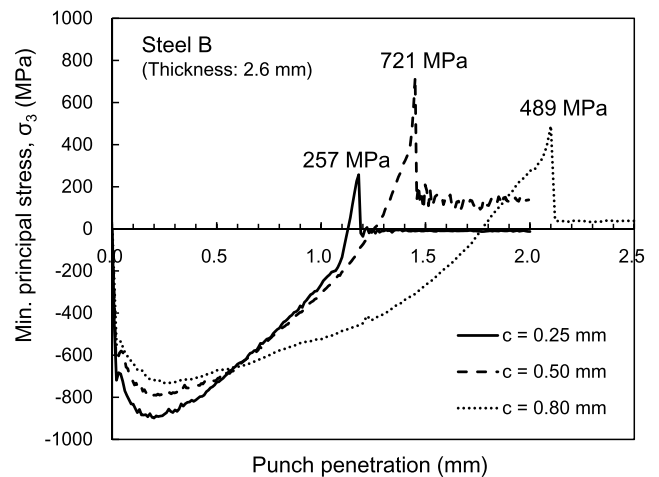

Fig. 16. Variations of minimum principal stress during punching process in steel B with clearances of 0.25 mm, 0.5 mm, and 0.8 mm.
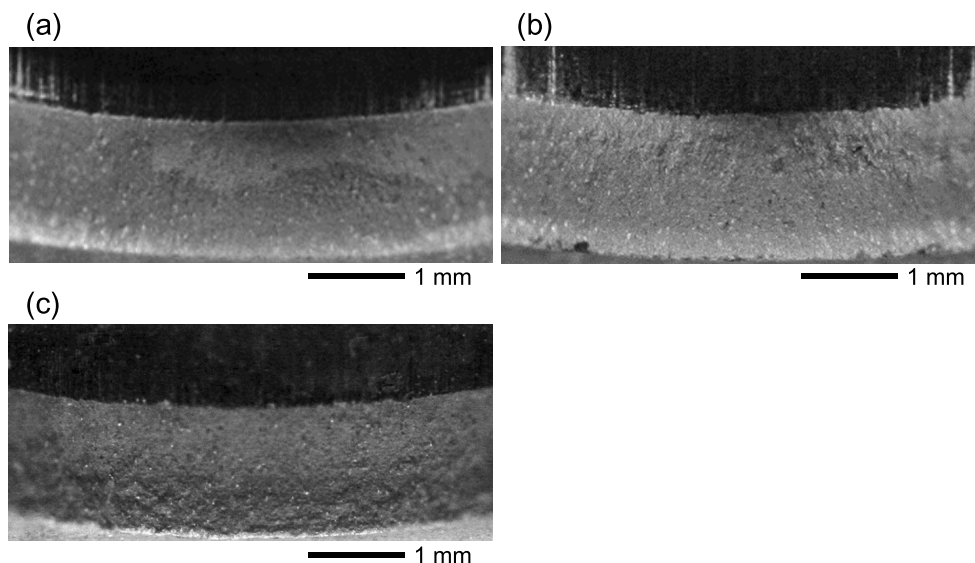

Fig. 17. Macrographs of shear edges of steel B punched with clearances of (a) 0.25 mm, (b) 0.8 mm, and shear edge of (c) steel A punched with clearance of 0.15 mm.

© 2020 ISIJ

The minimum lengths of the micro-ductile crack for cleavage fracture were calculated using Eq. (6) with the clearances of 0.25 mm and 0.8 mm. When the values of σ_3 were 257 MPa and 459 MPa, the minimum lengths of the micro-ductile cracks were determined to be 234 μm and 73 μm, respectively. The maximum lengths of the micro-ductile cracks observed in steel B punched with the clearance of 0.25 mm was 23 μm and punched with the clearance of 0.8 mm was 28 μm, which were significantly smaller than 234 μm and 73 μm. Therefore, formation of surface crack defects is considered difficult under the clearance conditions of 0.25 mm and 0.8 mm.

Figures 17(a) and 17(b) show the macrographs of the shear edge in steel B punched with the clearances of 0.25 mm and 0.8 mm. No surface crack defects were observed with the clearances of 0.25 mm and 0.8 mm, whereas occurrence of the surface crack defect was observed with the clearance of 0.5 mm, as shown in Fig. 2. The sheared edge condition was the smoothest with the clearance of 0.25 mm. Thus, the punching clearance strongly affects the formation of surface crack defects. Figure 17(c) shows the macrograph of the shear edge of steel A punched with the clearance of 0.15 mm. Surface crack defects were also suppressed in steel A by reducing the clearance from 0.5 mm to 0.15 mm.

6. Conclusions

The surface crack defects that develop on the shear edge in punching of the high-strength steel sheets were characterized by a round hole punching process. The formation mechanism can be described as follows:

(1) Surface crack defects were caused by cleavage fracture.

(2) Micro-ductile cracks with maximum lengths of 30 μm to 40 μm, which initiated at inclusions, were detected as pre-existing cracks in the material at the onset of material separation.

(3) The tensile stress perpendicular to the longitudinal direction of the micro-ductile crack developed within a period from the start to the end of material separation. This tensile stress can produce cleavage fracture when the micro-ductile crack satisfies a critical condition expressed by the Griffith equation.

(4) The tensile stress to produce surface crack defects increased in the material with higher yield strength, a higher strain hardening exponent, and a higher void nucleation rate.

(5) The tensile stress to produce surface crack defects also depended on the punching clearance, and it was shown experimentally that surface crack defects can be prevented by controlling the clearance appropriately.

REFERENCES

1) A. Dalloz, J. Besson, A. F. Gourgues-Lorenzon, T. Sturel and A. Pineau: *Eng. Fract. Mech.*, **76** (2009), 1411.
2) H. C. Shih, C. Chiriac and M. F. Shi: Proc. 2010 Int. Conf. on Manufacturing Science and Engineering (MSEC2010), ASME, New York, (2010), 599.
3) K. Tomita, T. Shiozaki, T. Urabe and K. Osawa: *Tetsu-to-Hagané*, **87** (2001), 557 (in Japanese).
4) T. Shiozaki, Y. Tamai and T. Urabe: *Int. J. Fatigue*, **80** (2015), 324.
5) T. Okano, K. Sakumoto, K. Yamazaki, S. Toyoda and S. Suzuki: *Key Eng. Mater.*, **716** (2016), 643.
6) R. Hambli: *Int. J. Mech. Sci.*, **43** (2001), 2769.
7) Y. Yoshida, Y. Murase, N. Yukawa and T. Ishikawa: *J. Jpn. Soc. Technol. Plast.*, **46** (2005), 392 (in Japanese).
8) Z. Yue, H. Badreddine, K. Saanouni, X. Zhuang and J. Gao: *Int. J. Damage Mech.*, **26** (2017), 1061.
9) O. León-García, R. Petrov and A. I. L. Kestens: *Mater. Sci. Eng. A*, **527** (2010), 4202.
10) A. S. Argon and J. Im: *Metall. Trans. A*, **6** (1975), 839.
11) D. Kwon and R. J. Asaro: *Metall. Trans. A*, **21** (1990), 117.
12) F. M. Beremin: *Metall. Trans. A*, **12** (1981), 723.
13) N. Ishikawa, D. M. Parks and M. Kurihara: *ISIJ Int.*, **40** (2000), 519.
14) F. Minami, C. Ruggieri, M. Ohata and M. Toyoda: *J. Soc. Mater. Sci. Jpn.*, **45** (1996), 544 (in Japanese).
15) P. Bennet and G. M. Sinclair: *J. Basic Eng.*, **88** (1966), 518.
16) D. A. Curry and J. F. Knott: *Met. Sci.*, **12** (1978), 511.
17) T. Lin, A. G. Evans and R. O. Ritchie: *Metall. Trans. A*, **18** (1987), 641.
18) T. L. Anderson: Fracture Mechanics: Fundamentals and Applications, 2nd ed., Talor & Francis, Oxford, (1995), 38.
19) J. I. San Martin and J. M. Rodriguez-Ibabe: *Scr. Mater.*, **40** (1999), 459.
20) J. R. Rice and D. M. Tracey: *J. Mech. Phys. Solids*, **17** (1969), 201.
21) A. L. Gurson: *J. Eng. Mater. Technol.*, **99** (1977), 2.
22) V. Tvergaard: *Int. J. Fract.*, **17** (1981), 389.
23) V. Tvergaard: *J. Mech. Phys. Solids*, **30** (1982), 265.
24) V. Tvergaard and A. Needleman: *Acta Metall.*, **32** (1984), 157.
25) Dassault Systems: ABAQUS 6.11 Documentation, User's Manual, (2011), 14-17, http://130.149.89.49:2080/v6.11/pdf_books/CAE.pdf, (accessed 2019-06-17).
26) T. Miyata, A. Otsuka, M. Mitsubayashi, T. Haze and S. Aihara: *J. Soc. Mater. Sci. Jpn.*, **37** (1988), 897 (in Japanese).
27) T. Tankoua, J. Crépin, P. Thibaux, S. Cooreman and A. F. Gourgues-Lorenzon: *Int. J. Fract.*, **212** (2018), 143.